Volume 2
Number 12
December 2020
Pages 5481–5914

Nanoscale Advances

rsc.li/nanoscale-advances

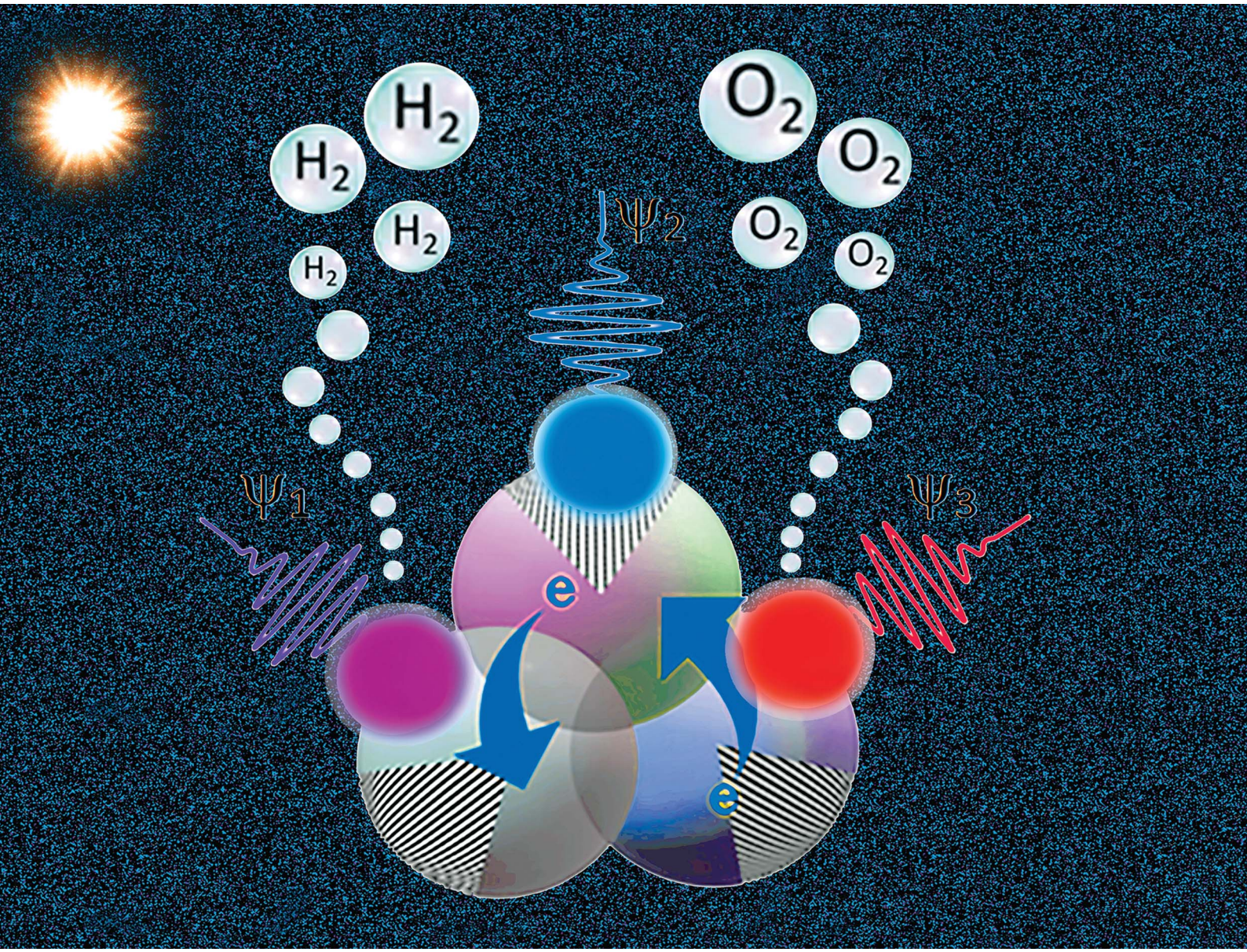

ISSN 2516-0230

ROYAL SOCIETY OF CHEMISTRY

PAPER

Vasudevanpillai Biju, Challapalli Subrahmanyam *et al.*
A photoanode with plasmonic nanoparticles of earth abundant bismuth for photoelectrochemical reactions

NCNST

Nanoscale Advances

ROYAL SOCIETY OF CHEMISTRY

PAPER

View Article Online
View Journal | View Issue

Cite this: *Nanoscale Adv.*, 2020, **2**, 5591

A photoanode with plasmonic nanoparticles of earth abundant bismuth for photoelectrochemical reactions†

Palyam Subramanyam,[a] Melepurath Deepa,[a] Sai Santosh Kumar Raavi,[a] Hiroaki Misawa,[bc] Vasudevanpillai Biju *[c] and Challapalli Subrahmanyam *[a]

A wide range of technologies has been developed for producing hydrogen economically and in greener ways. Photoelectrochemical water splitting using photoelectrodes submerged in a bath electrolyte forms a major route of hydrogen evolution. The efficacy of water splitting is improved by sensitizing metal oxide photoelectrodes with narrow bandgap semiconductors that efficiently absorb sunlight and generate and transport charge carriers. Here we show that the efficiencies of photocurrent generation and photoelectrochemical hydrogen evolution by the binary TiO_2/Sb_2S_3 anode increase by an order of magnitude upon the incorporation of the earth-abundant plasmonic bismuth nanoparticles into it. The ternary electrode TiO_2/Bi nanoparticle/Sb_2S_3 illuminated with sunlight provides us with a photocurrent density as high as 4.21 mA cm^{-2} at 1.23 V, which is fourfold greater than that of the binary electrode and tenfold greater than that of pristine TiO_2. By using bismuth nanoparticles, we estimate the incident photon to current conversion efficiency at 31% and solar power conversion efficiency at 3.85%. Here the overall impact of bismuth nanoparticles is attributed to increases in the open-circuit voltage (860 mV), which is by expediting the transfer of photogenerated electrons from Sb_2S_3 nanoparticles to the TiO_2 electrode, and short-circuit current (9.54 mA cm^{-2}), which is by the plasmonic nearfield effect. By combining the cost-effective plasmonic bismuth nanoparticles with the narrow bandgap Sb_2S_3 on the TiO_2 electrode, we develop a stable, ternary photoanode and accomplish high-efficiency photocurrent generation and hydrogen evolution.

Received 4th August 2020
Accepted 1st October 2020

DOI: 10.1039/d0na00641f

rsc.li/nanoscale-advances

Hydrogen is the most promising fuel for fulfilling the increasing global energy demand and cosseting the environmental costs of fossil fuels and greenhouse gases.[1–3] Photoelectrochemical (PEC) water splitting for hydrogen production is environmentally benign.[4–7] Even though TiO_2 is a promising and the most investigated n-type semiconductor photoelectrode for PEC water splitting, its efficiency to produce hydrogen is limited by the large bandgap (3.2 eV) or the absorption of UV radiation.[8–11] Therefore, TiO_2 is modified with narrow bandgap semiconductors such as CdS, $BiVO_4$ and Bi_2S_3, which is for extending the absorption edge to the visible and near infrared regions.[12–17] For example, an FTO/TiO_2/$BiVO_4$ heterojunction electrode provides higher PEC performance (4.11 mA cm^{-2} at 1.23 V) over FTO/TiO_2 or FTO/$BiVO_4$.[18] Similarly, heterojunction photoelectrodes composed of TiO_2 nanorods and Bi_2S_3 nanowires provide higher photocurrent density (2.4 mA cm^{-2} at 0.7 V *vs.* RHE) than pristine TiO_2.[19]

Along with the natural abundance of Sb_2S_3 and the large optical absorption coefficient, the high stability and narrow bandgap (1.7–1.8 eV) make it a promising co-sensitizer of TiO_2.[20–25] Liu *et al.*, used a WO_3/Sb_2S_3 heterojunction electrode and obtained four-fold enhancement of photocurrent density (1.79 mA cm^{-2} at 0.8 V) over pristine WO_3.[26] Also, Song *et al.* reported a current density of 0.79 mA cm^{-2} at an onset of −0.08 V for TiO_2/Sb_2S_3, while pristine TiO_2 shows poor performance under similar experimental conditions.[27] Nonetheless, such binary electrodes pose issues such as slow injection of electrons and high rates of carrier recombination. The efficiency of electron injection is improved by interfacing with noble metal nanoparticles (NPs) such as Ag and Au.[28–34] Here the metal NP not only lowers the rate of energy-wasting charge recombination in semiconductors but also enhances the photoreactivity due to the localized surface plasmon resonance (LSPR).[35–38] The collectively oscillating conduction band electrons in a plasmonic NP facilitate the absorption of a wide range of solar photons, which depends upon the metal

[a]*Department of Chemistry, Indian Institute of Technology, Kandi, Hyderabad, India-502285*

[b]*Center for Emergent Functional Matter Science, National Chiao Tung University, Taiwan*

[c]*Research Institute for Electronic Science, Hokkaido University, N20 W10, Sapporo, Hokkaido 001-0020, Japan. E-mail: biju@es.hokudai.ac.jp*

† Electronic supplementary information (ESI) available. See DOI: 10.1039/d0na00641f

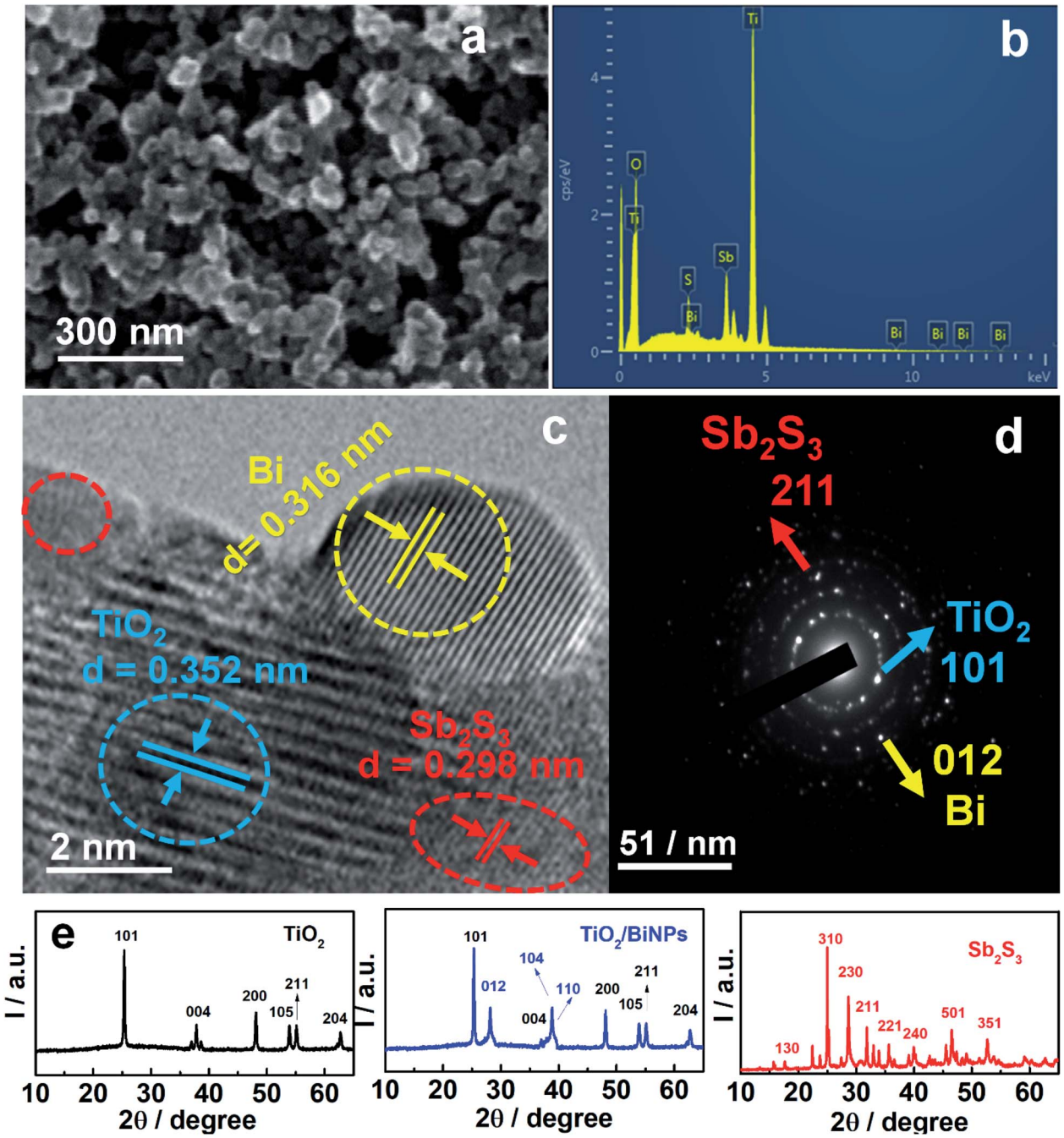

Fig. 1 Characterization of the ternary photoanode and anode materials. (a) FESEM image, (b) EDAX image, (c) HR-TEM image and (d) SAED pattern of TiO_2/BiNP/Sb_2S_3, and (e) XRD patterns of TiO_2, TiO_2/BiNP and Sb_2S_3.

as well as the size and shape of the NP. As an example, CdS/Ag/ZnO photoanodes show higher (3.13%) solar energy conversion efficiency than CdS/ZnO alone (1.35%).[39] Also, Li *et al.*, fabricated CdS/Au/TiO_2 photoanodes and achieved photocurrent density as high as 4.07 mA cm^{-2} at 0 V *vs.* the Ag/AgCl electrode.[40] Although bismuth (Bi) NPs expand the optical absorption window and suppress the rate of carrier recombination in conventional semiconductors,[41–46] the plasmonic properties of this earth-abundant NP[41] are yet to be explored in PEC applications.

We report the ternary photoanode TiO_2/BiNP/Sb_2S_3 and its application in high efficiency PEC water splitting. The electrode is prepared by chemical bath deposition (CBD). We accomplish an order of magnitude higher efficiency of PEC hydrogen evolution by supplementing the conventional TiO_2 electrode with the narrow bandgap Sb_2S_3 and the plasmonic properties of BiNPs. The ternary electrode provides us with a photocurrent density as high as 4.21 mA cm^{-2} at 1.23 V, the incident photon to current conversion efficiency (IPCE) at 31%, and solar power conversion efficiency at 3.85%. We hypothesize that BiNPs

enhance the open circuit voltage by bending the band across the junctions, expediting the transfer of photogenerated electrons from Sb_2S_3 to TiO_2, and increase the short circuit current by the SPR effect.

The ternary photoanode TiO_2/BiNP/Sb_2S_3 was prepared by the doctor-blade technique and chemical bath deposition. The details of photoanode fabrication are provided in the Experimental section. The ternary electrode and BiNPs were characterized by FESEM, EDAX, HRTEM, Raman spectroscopy and XRD studies. Fig. 1a shows the surface morphology of the photoanode TiO_2/BiNP/Sb_2S_3, which aggregate randomly with no specific shape displaying high roughness. Further, the EDAX image confirms that the constituent elements in the ternary electrode are Ti, O, Bi, Sb and S (Fig. 1b) and it reveals that BiNPs are effectively incorporated on TiO_2 in the composite. The SEM and EDAX images of BiNPs, TiO_2/BiNP and TiO_2/Sb_2S_3 are shown in Fig. S1.† Further, the HRTEM image of the TiO_2/BiNP/Sb_2S_3 photoanode reveals the placement of BiNPs in between TiO_2 and Sb_2S_3 and the lattice fringes of individual components (Fig. 1c). Body centered tetragonal TiO_2 has a lattice spacing of 0.352 nm that corresponds to (101) (JCPDS-894921), while orthorhombic Sb_2S_3 has a lattice constant of 0.298 nm that is assigned to the (211) plane (JCPDS-421393). Plasmonic BiNPs have a lattice spacing of 0.316 nm which is assigned to the (012) plane (JCPDS-851331). The selected area electron diffraction (SAED) patterns (Fig. 1d) confirm the crystalline structures of BiNP, TiO_2 and Sb_2S_3. The TEM images of pure BiNPs show a spherical shape with an average particle size of around 5–10 nm (Fig. S2a†) and the lattice spacing of 0.32 nm relates to the (012) plane of Bi (JCPDS-851331) (Fig. S2b†). The XRD pattern of pure BiNPs is shown in the ESI (Fig. S2c†) and BiNPs possess a rhombohedral structure with the (012), (104), (110) and (202) planes corresponding to *d*-spacings of 3.25, 2.34, 2.24 and 1.83 Å respectively (JCPDS: 851331). No peaks of other bismuth compounds (such as Bi_2O_3) can be observed in the pattern which suggests that Bi^{3+} ions reduced to metallic Bi.[42,44,49] The XRD patterns of TiO_2, TiO_2/BiNP and Sb_2S_3 are shown in Fig. 1e, which demonstrate the body-centered tetragonal crystal lattice of TiO_2, rhombohedral structure of BiNPs and orthorhombic primitive lattice of Sb_2S_3. TiO_2 has a body-centered tetragonal crystal lattice with the (101), (103), (004), (200), (105), (211) and (204) planes corresponding to *d*-spacings of 3.51, 2.43, 2.36, 1.89, 1.69, 1.66, 1.47 and 1.36 Å respectively (JCPDS-894921). In TiO_2/BiNP, the presence of (012), (104) and (110) planes, confirms formation of TiO_2/BiNPs. Sb_2S_3 has an orthorhombic primitive lattice with the (130), (310), (230), (211), (221), (240), (501) and (351) planes corresponding to *d*-spacings of 3.54, 3.49, 3.16, 3.01, 2.74, 2.55, 1.93 and 1.73 Å respectively (JCPDS: 421393). Raman spectral analysis of BiNPs is shown in Fig. S2d,† where pure BiNPs show two characteristic vibrational bands at 68 and 91 cm^{-1} corresponding to E_g and A_{1g} modes respectively. Furthermore, the Raman spectra of TiO_2, TiO_2/BiNP and TiO_2/BiNP/Sb_2S_3 (Fig. S3†) help us to clarify the structures of the electrode components. The anatase phase of TiO_2 was confirmed by the Raman bands at 144 and 635 cm^{-1} that correspond to the E_g mode while 396 and 512 cm^{-1} belong to B_{1g} and B_{1g}/A_{1g} modes respectively. In TiO_2/BiNP, the presence of peaks at 68 and 91 cm^{-1}, confirms that BiNPs are well incorporated with TiO_2 particles. Further, the introduction of Sb_2S_3 onto TiO_2/BiNP, shows peaks at 135, 188 and 431 cm^{-1} that belong to the vibrational modes of SbS_3 units and Sb–Sb bonds in Sb_2S_3 respectively. The Raman spectra of a pure Sb_2S_3 sample are displayed in Fig. S4.†

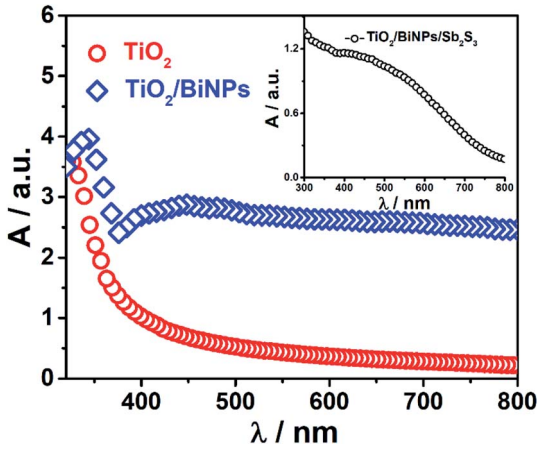

Fig. 2 Absorption spectra of the TiO_2 and TiO_2/BiNP electrodes. Inset: absorption spectrum of the TiO_2/BiNP/Sb_2S_3 electrode.

With the modification of the TiO_2 electrode using BiNPs and Sb_2S_3 sensitizers, the absorption band of the electrode extends from the UV to NIR region. Fig. 2 shows the absorption spectra of TiO_2, TiO_2/BiNP and TiO_2/BiNP/Sb_2S_3 electrodes, which reveal the strong absorption of light in the range of 400–800 nm by BiNPs. This corresponds to near UV to NIR absorption, which is confirmed by the absorption spectra of an aqueous solution of pure BiNPs (Fig. S5a and b†). The broad absorption in the UV-Vis-NIR region (Fig. 2) is due to the SPR of BiNPs.[49,50] The TiO_2 electrode selectively absorbs light with a wavelength smaller than 390 nm. The absorption onset of TiO_2 is expanded to the 400–750 nm region with the chemical bath deposition of the small bandgap Sb_2S_3 (Fig. S4b†). The bandgaps of TiO_2 and Sb_2S_3 employed in this work are estimated at 3.13 and 1.6 eV, respectively.

To evaluate the plasmonic effect of BiNPs on the PEC activity of the ternary electrode, we examined the photocurrent response by each photoanode (TiO_2 alone, TiO_2/Sb_2S_3 or TiO_2/BiNP/Sb_2S_3) by linearly sweeping the voltage (LSV plots) in a three-electrode system (Ag/AgCl as the reference electrode and Pt as the counter electrode), and the results are summarized in Fig. 3a. The pH of the electrolyte was set at 12.7 and the cells are illuminated with simulated sunlight (AM1.5). All the potentials reported against the reversible hydrogen electrode (RHE) are calculated using the Nernst equation. Upon chopped light illumination, the photocurrent density values for TiO_2, TiO_2/BiNP, TiO_2/Sb_2S_3 and TiO_2/BiNP/Sb_2S_3 photoanodes are 0.15, 0.61, 1.83 and 4.21 mA cm^{-2}, respectively, at 1.23 V. The highest photo-response in terms of current density is observed for TiO_2/BiNP/Sb_2S_3 at the lowest onset potential of 0.13 V. The enhanced photocurrent density of the TiO_2/BiNP/Sb_2S_3 electrode, which is promising for PEC water splitting, is attributed

to the ability of Sb_2S_3 to absorb the visible-NIR light and the SPR of BiNPs. In addition, the efficiency of a photoelectrode is expressed in terms of solar to hydrogen conversion (STH). The STH conversion efficiencies for TiO_2, TiO_2/BiNP, TiO_2/Sb_2S_3 and TiO_2/BiNP/Sb_2S_3 are estimated at 0.03, 0.22, 0.51 and 1.56% at 0.6 V (Fig. 3b), which are calculated from short circuit current density and the intensity of incident light (ESI†). The TiO_2/BiNP/Sb_2S_3 photoanode provides us with 3- and 15-times higher STH conversion efficiency than TiO_2/Sb_2S_3 and TiO_2, respectively. Furthermore, estimation of the PEC water splitting performance of the TiO_2/Sb_2S_3/BiNP electrode was carried out by using LSV plots and the results are presented in Fig. S6a.† Upon chopped light illumination, the TiO_2/Sb_2S_3/BiNP electrode showed a maximum photocurrent density of 3.16 mA cm^{-2} at 1.23 V. Further, the high STH conversion efficiency of the TiO_2/Sb_2S_3/BiNP electrode is 0.68% at 0.6 V (Fig. S6b†). Therefore, the TiO_2/Sb_2S_3/BiNP electrode provides lower photocurrent density and STH efficiency than the TiO_2/Bi/Sb_2S_3 electrode. These results suggested that BiNP-embedded TiO_2/Sb_2S_3 can be better understood based on the staggered energy alignment of the TiO_2/Bi/Sb_2S_3 compared to BiNPs grown on the surface of Sb_2S_3 (TiO_2/Sb_2S_3/BiNP) for improving PEC water splitting.

The stability of the photocurrent response by TiO_2, TiO_2/BiNP, TiO_2/Sb_2S_3 and TiO_2/BiNP/Sb_2S_3 photoanodes is examined by chronoamperometric (*I–t* curve) studies. Also, the photocurrent responses of the electrodes are tested at 1.23 V *versus* RHE (0.6 *versus* Ag/AgCl) under simulated solar (AM1.5) irradiation, and the results are presented in Fig. 3c. The long-term stability of the ternary electrode is noteworthy; only little decay in performance is observed after 5100 s. H_2 evolution is quantified using gas chromatography and the amount of H_2 evolved is plotted as a function of time at 1.23 V *vs.* RHE. As shown in Fig. 3d, the TiO_2/BiNP/Sb_2S_3 photoanode provides maximum (3.2 mmol) H_2 evolution over 2 h, which is when compared to TiO_2/Sb_2S_3. The high photocurrent efficiency and H_2 evolution performances of TiO_2/BiNP/Sb_2S_3 are in good agreement.

The ability of photoelectrodes to convert the incident photons into electrons is examined by IPCE experiments in

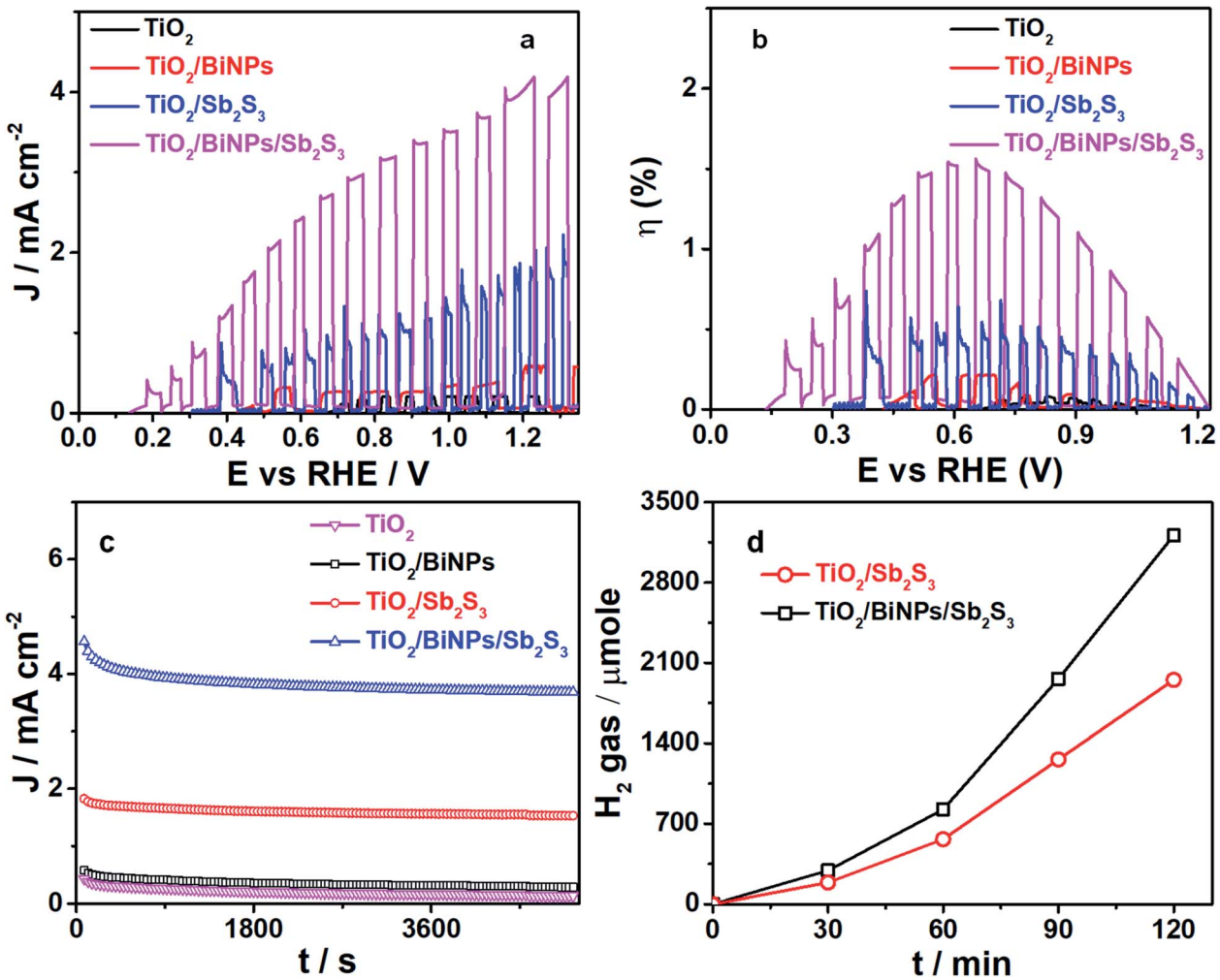

Fig. 3 PEC properties of photoanodes. (a) LSV plots, (b) solar to hydrogen conversion efficiency and (c) photocurrent stability plots of TiO_2, TiO_2/BiNP, TiO_2/Sb_2S_3 and TiO_2/BiNP/Sb_2S_3 electrodes. Here 0.1 M Na_2SO_3 and 0.1 M Na_2SO_4 are used as the electrolyte solution under simulated solar irradiation. (d) Temporal evolution of H_2 gas by TiO_2/Sb_2S_3 and TiO_2/BiNP/Sb_2S_3 electrodes.

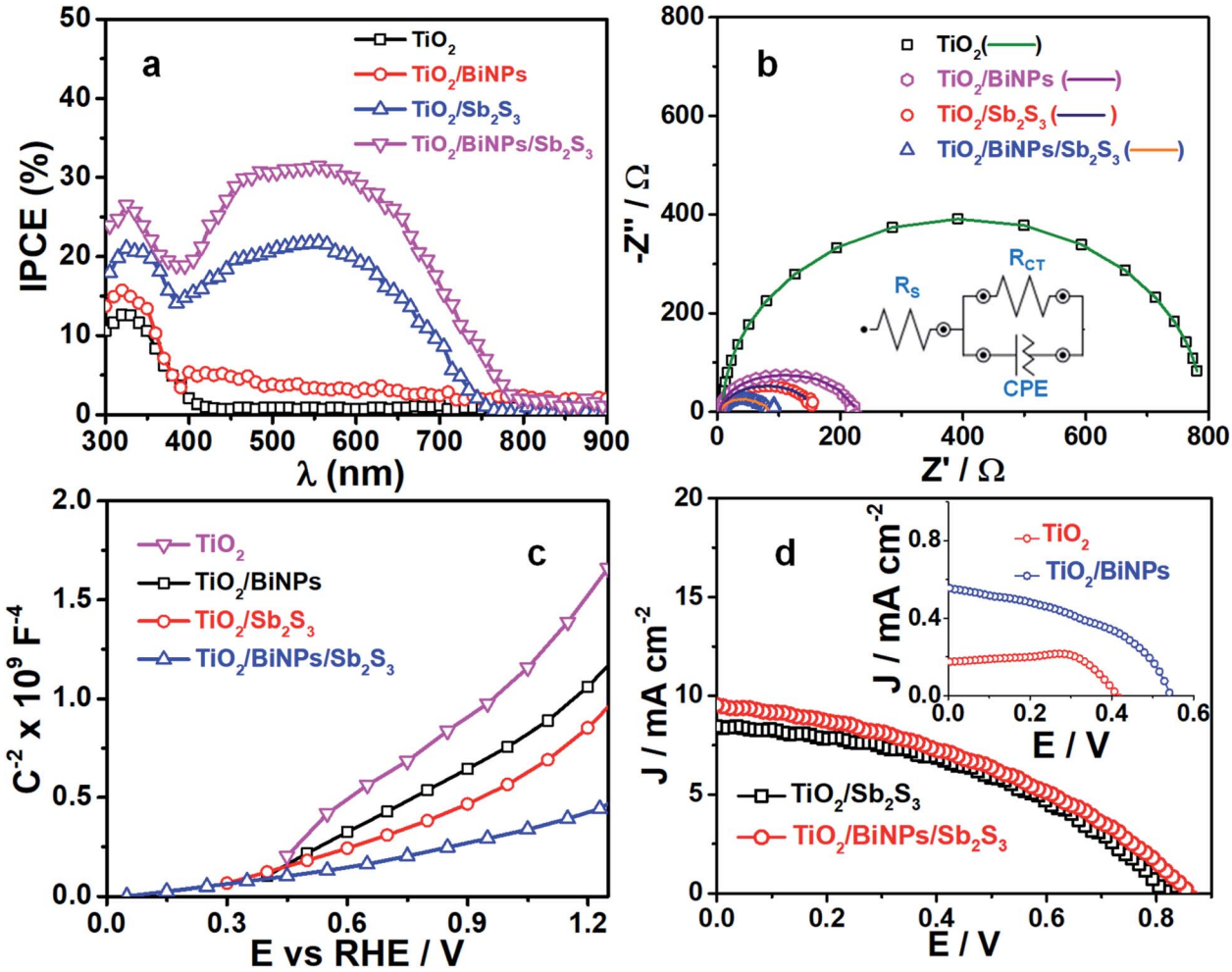

Fig. 4 IPCE and *I*/*V*/*R* characteristics of photoanodes. (a) Wavelength-dependent IPCE plots (b) Nyquist plots (symbol) with an equivalent circuit (dot lines) and (c) Mott–Schottky plots of pristine TiO_2, TiO_2/BiNP, TiO_2/Sb_2S_3 and TiO_2/BiNP/Sb_2S_3 photoanodes. (d) *J*–*V* data of TiO_2/Sb_2S_3 and TiO_2/BiNP/Sb_2S_3 photoanodes.

a two-electrode system, but without applying any external bias, as shown in Fig. 4a. The maximum IPCE for TiO_2 is 13% in the UV region (300–400 nm), which is negligibly small in the visible to NIR region (400–900 nm). We find an increase in the IPCE for the TiO_2 electrode supplemented with BiNPs, which is 15% in the UV region (300–400 nm) and additional contribution of 2–5% in the 400–800 nm region. This enhancement in IPCE performance by BiNPs is attributed to their SPR in the visible to NIR region. When compared to the 13% IPCE of TiO_2 alone, the TiO_2/Sb_2S_3 electrode shows *ca.* 20% IPCE in the 300–750 nm region, which is attributed to the small bandgap of Sb_2S_3. Thus, by combining the plasmonic effect of BiNPs with the small bandgap of Sb_2S_3 in TiO_2/BiNP/Sb_2S_3, we accomplish 31% IPCE for the ternary photoanode. Also, this result implies that BiNPs in the heterojunction suppress undesired recombination of photogenerated charge carriers in Sb_2S_3.

The kinetics of charge injection at the photoanode/electrolyte interfaces are studied by measuring the resistance across the electrode/electrolyte interface. Here impedance measurements were carried out under the light illumination of TiO_2, TiO_2/BiNP, TiO_2/Sb_2S_3 or TiO_2/BiNP/Sb_2S_3 electrodes immersed in a solution of 0.1 M Na_2SO_3 and 0.1 M Na_2SO_4 (1 : 1, v/v) and the plots were fitted into the equivalent circuits shown in the inset in Fig. 4b, where R_S, R_{CT} and CPE represent the electrolyte solution resistance, interfacial charge transfer resistance at electrode/electrolyte and constant phase element for photoelectrode/electrolyte, respectively. The fitted parameters are given in Table 2 (ESI†). All the electrodes have solution resistance (R_S) in the range of 4–9 Ω. The high R_{CT} value of 775 Ω for TiO_2 is due to low charge separation and the lowest R_{CT} value of 71 Ω is observed for the TiO_2/BiNP/Sb_2S_3 photoanode compared to other electrodes, indicating the facile transfer of charge carriers at the TiO_2/BiNP/Sb_2S_3 photoanode/electrolyte interface, which is consistent with the excellent PEC performance of the electrode. Also, these charge injection properties are consistent with the electron lifetime (τ) values estimated from Bode plots (Fig. S7†). The τ values are estimated using the relation $\tau = 1/(2\pi f_{max})$ where f_{max} is the frequency maxima. The τ values calculated for pristine TiO_2, TiO_2/BiNP, TiO_2/Sb_2S_3 and TiO_2/BiNP/Sb_2S_3 films are 1.13, 1.22, 1.46 and 1.65 ms,

respectively. The large τ value corresponds to a high rate of carrier transport or low rate of undesired carrier recombination in the TiO_2/BiNP/Sb_2S_3 photoelectrode, which is attributed to the effect of BiNPs. In other studies, BiNPs increase the τ value of TiO_2/BiNP/Sb_2S_3, which is in good agreement with the higher photocurrent density. Furthermore, we construct the Mott–Schottky plots of electrodes (Fig. 4c), where the linear profiles with positive slopes confirm the n-type characteristics of the photoanodes.

To evaluate the role of plasmonic BiNPs on the power conversion efficiency of the ternary electrode, we constructed different photoelectrochemical solar cells and recorded the current–voltage (J–V) characteristics of the cells under 1 sun illumination (100 mW cm^{-2}). Here the electrolyte used was polysulfide (0.1 M Na_2S and 0.1 M S) solution. The active area of the working electrode (TiO_2, TiO_2/Sb_2S_3, or TiO_2/BiNP/Sb_2S_3) was set at 0.15 cm^2, and the counter electrode used was C-fabric. The J–V responses of the cells are shown in Fig. 4d and the solar cell parameters are summarized in Table S1 (ESI†). The TiO_2/BiNP/Sb_2S_3 cell shows an open circuit voltage (V_{OC}) of ~860 mV and a short circuit current density (J_{SC}) of 9.54 mA cm^{-2}, which are greater than those of the TiO_2/Sb_2S_3 electrode. The power conversion efficiency (PCE) of cells with TiO_2, TiO_2/Bi, TiO_2/Sb_2S_3 and TiO_2/BiNP/Sb_2S_3 electrodes is 0.019, 0.39, 2.99 and 3.85% respectively. The TiO_2/BiNP/Sb_2S_3 based cells achieved the highest PCE and V_{OC} was also the highest for this cell compared to the other electrodes. The high value of V_{OC} is attributed to the bending of bands and improvement of charge separation induced by BiNPs. We attribute the high J_{SC} value to the SPR effect of BiNPs, which increases the carrier density. These NPs not only transfer the photogenerated electrons from Sb_2S_3 to FTO *via* TiO_2 but also act as photosensitizers, which are obvious from the high J_{SC} and V_{OC} values of FTO/TiO_2/BiNP when compared with FTO/TiO_2. The J–V characteristics FTO-based electrodes are shown in the inset in Fig. 4d. Furthermore, the higher PCE (0.39%) of the FTO/TiO_2/BiNP electrode, which is when compared with FTO/TiO_2 (0.01%), suggests that BiNPs transfer photogenerated electrons to the external circuit. In addition, the TiO_2/Bi electrode shows high J_{SC} (0.56 mA cm^{-2}) and V_{OC} (0.54 V) compared to the pure TiO_2 film which is due to different regions of the solar spectrum being absorbed and converted to current.

The Fermi level of BiNPs, and conduction (CB) and valence band (VB) positions of TiO_2 and Sb_2S_3 are obtained from cyclic voltammetry (Fig. S8†). The procedure for calculations of band positions in the energy level diagram is as shown in the ESI.† The mechanism of PEC performance of the ternary photoanode TiO_2/BiNP/Sb_2S_3 is schematically presented in Fig. 5. Here the simulated solar illumination of the electrode leads to the generation of electron/hole pairs in the conduction (CB)/valence bands (VB) of Sb_2S_3. The photogenerated holes in the VB of Sb_2S_3 react with the sacrificial reagent (SO_3^{2-}) and hydroxyl ion to produce SO_4^{2-} and oxygen. On the other hand, BiNPs assist the transport of photogenerated electrons through the external circuit to the counter electrode (Pt) where protons are reduced to liberate hydrogen. In this hypothetical mechanism, the primary role of BiNPs is to expedite the transfer of electrons from the conduction band of Sb_2S_3 to that of TiO_2 and finally to the back contact FTO.

In summary, by combining the low bandgap Sb_2S_3 with the plasmonic BiNPs in the ternary TiO_2/BiNP/Sb_2S_3 photoanode, we find that the efficiencies of photocurrent generation and photoelectrochemical hydrogen evolution increase by an order of magnitude when compared with the pristine TiO_2 electrode. This ternary photoanode shows photocurrent density as high as 4.21 mA cm^{-2} at 1.23 V with a solar to hydrogen conversion efficiency of 1.56% at 0.6 V. BiNPs deliver the SPR effect to Sb_2S_3 and increase the rate of electron transport from Sb_2S_3 to TiO_2, and as a result, the maximum of IPCE becomes 31% and the solar power conversion efficiency becomes 3.85%. By expediting the transfer of photogenerated electrons from Sb_2S_3 to the TiO_2 electrode, BiNPs increase the open circuit voltage up to 860 mV. Also, with the plasmonic nearfield effect, the short circuit current reaches up to 9.54 mA cm^{-2}. Overall, by combining the earth-abundant and cost-effective plasmonic BiNPs and the narrow bandgap Sb_2S_3 on the TiO_2 electrode, we develop a stable, ternary photoanode and accomplish high efficiency photocurrent generation and hydrogen evolution.

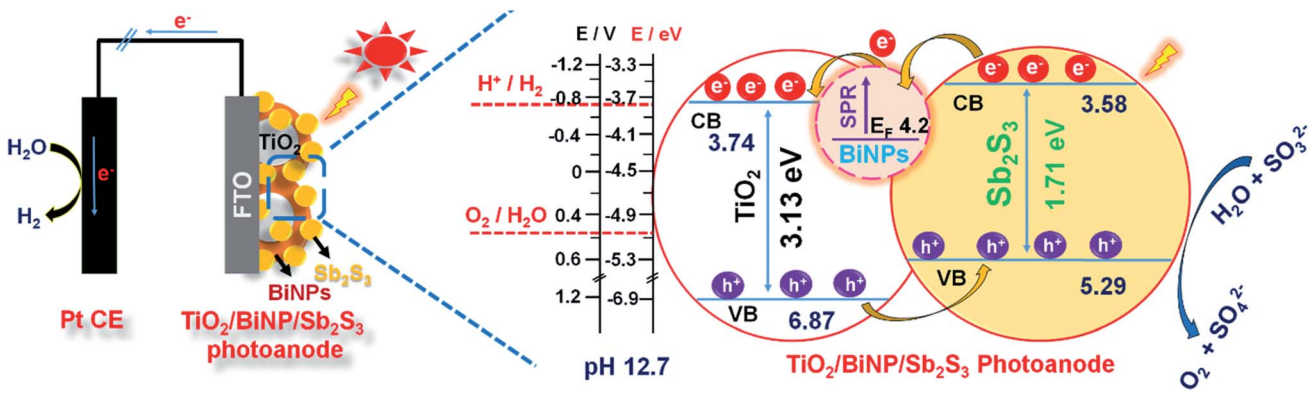

Fig. 5 A scheme of a PEC cell constructed using the ternary photoanode TiO_2/BiNP/Sb_2S_3, showing the band alignment, charge transport and redox reactions under the simulated solar irradiation.

Experimental

Materials and samples

Antimony chloride ($SbCl_3$), sodium thiosulfate ($Na_2S_2O_3$), bismuth nitrate pentahydrate [$Bi(NO_3)_3 \cdot 5H_2O$], dimethyl sulfoxide (DMSO), sodium sulfate (Na_2SO_4), elemental sulfur, methanol and acetone were obtained from Aldrich. Titanium tetrachloride ($TiCl_4$), sodium borohydride ($NaBH_4$), sodium sulfide (Na_2S), sodium sulfite (Na_2SO_3) and tannic acid were obtained from Merck. TiO_2 paste (18NR-T) used for electrode preparation was obtained from Dyesol. Deionized water (resistivity $\sim$ 18.2 Ω cm) was obtained from a Millipore Direct-Q3 UV system. Fluorine doped tin oxide (FTO) glass (sheet resistance $\sim$ 25 Ω cm^{-2}) was obtained from Pilkington.

Preparation of photoanodes

The TiO_2/BiNP/Sb_2S_3 ternary photoanode was prepared by the doctor-blade technique. The photoanode was fabricated as follows: TiO_2 paste was coated onto the pre-cleaned FTO substrates by the doctor-blade method, which was followed by annealing the TiO_2 film at 500 °C for 30 min to provide a thin layer of TiO_2 on FTO. Further, the TiO_2 film was immersed in a hot (70 °C) solution (40 mM in isopropanol) of $TiCl_4$ for 30 min. The film was rinsed with DI water and annealed at 500 °C for 30 min to provide the uniform TiO_2 electrode. Further, BiNPs were grown onto the TiO_2 electrode. In brief, $Bi(NO_3)_3 \cdot 5H_2O$ was dissolved in DMSO and a solution containing a mixture of $NaBH_4$ and tannic acid was slowly added, which brought about the reduction of Bi^{3+} to Bi^0 and the obtained BiNPs were dispersed in water for further studies. Finally, the TiO_2 film was vertically introduced into the bismuth precursor solution and sonicated for 15 min to form the TiO_2/BiNP film, which was brown in color. Further, Sb_2S_3 was grown onto the TiO_2/BiNP film by the chemical bath deposition process to form the ternary electrode TiO_2/BiNP/Sb_2S_3.[47,48] Briefly, 400 mg of $SbCl_3$ was dissolved in 2.5 mL of acetone, which was followed by the addition of 72.5 mL of deionized water to yield a turbid solution that subsequently converted into a white precipitate. Subsequently, 3.95 g of $Na_2S_2O_3$ dissolved in 25 mL of water was added to the $SbCl_3$ solution under stirring. The TiO_2/BiNP film was vertically dipped in the Sb_2S_3 solution at 25 °C for 60 min, which was followed by rinsing the electrode with deionized water and drying on a hot plate at 60 °C. Finally, the film was annealed at 300 °C for 15 min under an argon atmosphere to yield the dark-orange colored TiO_2/BiNP/Sb_2S_3 photoanode. Preparation of the electrode is illustrated in the ESI.†

Characterization techniques

The surface morphologies of the samples were analyzed using a field emission scanning electron microscope (FESEM-Zeiss supra 40). High-resolution transmission electron microscope (HR-TEM) images were recorded using a TECNAI G-2 FEI instrument operating at 300 kV. The powder X-ray diffraction (XRD) patterns of samples were measured on a PANalytical, Xpert PRO instrument. The Raman spectra of photoanode materials were recorded by using a Bruker Senterra dispersive Raman microscope spectrometer with an excitation wavelength of 532 nm. The absorption spectra of the synthesized electrodes were recorded on a UV-Vis spectrophotometer (Shimadzu UV-3600). PEC measurements were performed in an aqueous electrolyte containing a 1 : 1 mixture of 0.1 M Na_2SO_3 and 0.1 M Na_2SO_4, using a three electrode system with Pt and Ag/AgCl as the counter and reference electrodes, respectively. The current *versus* potential (*I–V*) characteristics of photoanodes were recorded using a LOT-Oriel-Autolab with a 150 W xenon arc lamp with 100 mW cm^{-2} intensity. Chronoamperometric (*I–t*) plots, Mott–Schottky plots, cyclic voltammetry (CV) and electrochemical impedance spectra (EIS) were measured on an Autolab PGSTAT 302N equipped with NOVA 1.9 software. The irradiance intensity was confirmed by calibrating with a 2 cm $\times$ 2 cm Si Reference Cell and re-affirmed with a radiant power meter from Newport (842-PE). The IPCE was measured using a quantum efficiency measurement system (Oriel IQE-200), where 250 W quartz tungsten and halogen lamps were used as the light sources, the monochromator path length was 1/8M and the spot size was 1 mm $\times$ 2.5 mm rectangular at focus. This instrument gave the IPCE values as a function of wavelength directly.

Conflicts of interest

There are no conflicts to declare.

Acknowledgements

PS thanks CSIR-HRDG, New Delhi for providing fellowship. CS, SSKR and VB acknowledge the financial support under the SPARC program of the Science and Engineering Research Board of India. VB acknowledges financial support under the MEXT JSPS Grant-in-Aid for Scientific Research B (19H02550). HM and VB acknowledge financial support under the MEXT JSPS Special Advancement Research Grant (18H05205).

References

1 M. G. Walter, E. L. Warren, J. R. McKone, S. W. Boettcher, Q. Mi, E. A. Santori and N. S. Lewis, Solar water splitting cells, *Chem. Rev.*, 2010, **110**, 6446–6473.
2 Y. Tachibana, L. Vayssieres and J. R. Durrant, Artificial photosynthesis for solar water-splitting, *Nat. Photonics*, 2012, **6**, 511.
3 S. Y. Tee, K. Y. Win, W. S. Teo, L. D. Koh, S. Liu, C. P. Teng and M. Y. Han, Recent progress in energy-driven water splitting, *Adv. Sci.*, 2017, **4**, 1600337.
4 S. C. Warren, K. Voïtchovsky, H. Dotan, C. M. Leroy, M. Cornuz, F. Stellacci, C. Hébert, A. Rothschild and M. Grätzel, Identifying champion nanostructures for solar water-splitting, *Nat. Mater.*, 2013, **12**, 842.
5 M. Grätzel, Photoelectrochemical cells, *Nature*, 2001, **414**, 338.
6 E. L. Miller, Photoelectrochemical water splitting, *Energy Environ. Sci.*, 2015, **8**, 2809–2810.

7 K. Sivula and R. Van De Krol, Semiconducting materials for photoelectrochemical energy conversion, *Nat. Rev. Mater.*, 2016, **1**, 15010.
8 A. Fujishima and K. Honda, Electrochemical photolysis of water at a semiconductor electrode, *Nature*, 1972, **238**, 37.
9 G. Wang, H. Wang, Y. Ling, Y. Tang, X. Yang, R. C. Fitzmorris, C. Wang, J. Z. Zhang and Y. Li, Hydrogen-treated TiO_2 nanowire arrays for photoelectrochemical water splitting, *Nano Lett.*, 2011, **11**, 3026–3033.
10 I. S. Cho, Z. Chen, A. J. Forman, D. R. Kim, P. M. Rao, T. F. Jaramillo and X. Zheng, Branched TiO_2 nanorods for photoelectrochemical hydrogen production, *Nano Lett.*, 2011, **11**, 4978–4984.
11 S. Liang, J. He, Z. Sun, Q. Liu, Y. Jiang, H. Cheng, B. He, Z. Xie and S. Wei, Improving photoelectrochemical water splitting activity of TiO_2 nanotube arrays by tuning geometrical parameters, *J. Phys. Chem. C*, 2012, **116**, 9049–9053.
12 P. Pathak, S. Gupta, K. Grosulak, H. Imahori and V. Subramanian, Nature-inspired tree-like TiO_2 architecture: a 3D platform for the assembly of CdS and reduced graphene oxide for photoelectrochemical processes, *J. Phys. Chem. C*, 2015, **119**, 7543–7553.
13 P. Subramanyam, P. N. Kumar, M. Deepa, C. Subrahmanyam and P. Ghosal, Bismuth sulfide nanocrystals and gold nanorods increase the photovoltaic response of a TiO_2/CdS based cell, *Sol. Energy Mater. Sol. Cells*, 2017, **159**, 296–306.
14 X. Wang, J. Xie and C. M. Li, Architecting smart "umbrella" Bi_2S_3/rGO-modified TiO_2 nanorod array structures at the nanoscale for efficient photoelectrocatalysis under visible light, *J. Mater. Chem. A*, 2015, **3**, 1235–1242.
15 P. Subramanyam, T. Vinodkumar, M. Deepa and C. Subrahmanyam, Gold nanoparticle decorated bismuth sulfide nanorods for enhanced photoelectrochemical hydrogen production, *J. Mater. Chem. C*, 2019, **7**, 6398–6405.
16 D. V. Freitas, J. R. González-Moya, T. A. Soares, R. R. Silva, D. M. Oliveira, H. S. Mansur, G. Machado and M. Navarro, Enhanced visible-light photoelectrochemical conversion on TiO_2 nanotubes with Bi_2S_3 quantum dots obtained by in situ electrochemical method, *ACS Appl. Energy Mater.*, 2018, **1**, 3636–3645.
17 S. Ho-Kimura, S. J. Moniz, A. D. Handoko and J. Tang, Enhanced photoelectrochemical water splitting by nanostructured $BiVO_4$–TiO_2 composite electrodes, *J. Mater. Chem. A*, 2014, **2**, 3948–3953.
18 H. Zhang and C. Cheng, Three-dimensional FTO/TiO_2/$BiVO_4$ composite inverse opals photoanode with excellent photoelectrochemical performance, *ACS Energy Lett.*, 2017, **2**, 813–821.
19 C. Liu, Y. Yang, W. Li, J. Li, Y. Li and Q. Chen, A novel Bi_2S_3 nanowire@TiO_2 nanorod heterogeneous nanostructure for photoelectrochemical hydrogen generation, *Chem. Eng. J.*, 2016, **302**, 717–724.
20 J. Zhong, X. Zhang, Y. Zheng, M. Zheng, M. Wen, S. Wu, J. Gao, X. Gao, J. M. Liu and H. Zhao, High efficiency solar cells as fabricated by Sb_2S_3-modified TiO_2 nanofibrous networks, *ACS Appl. Mater. Interfaces*, 2013, **5**, 8345–8350.
21 H. Du, C. Yang, W. Pu, H. Zhao and J. Gong, Highly active Sb_2S_3 attached Mo–WO_3 composite film for enhanced photoelectrocatalytic water splitting at extremely low input light energy, *ACS Sustainable Chem. Eng.*, 2019, **7**, 9172–9181.
22 A. D. DeAngelis, K. C. Kemp, N. Gaillard and K. S. Kim, Antimony(III) sulfide thin films as a photoanode material in photocatalytic water splitting, *ACS Appl. Mater. Interfaces*, 2016, **8**, 8445–8451.
23 Z. Yang, X. Wang, Y. Chen, Z. Zheng, Z. Chen, W. Xu, W. Liu, Y. M. Yang, J. Zhao, T. Chen and H. Zhu, Ultrafast self-trapping of photoexcited carriers sets the upper limit on antimony trisulfide photovoltaic devices, *Nat. Commun.*, 2019, **10**, 1–8.
24 Y. Wu, L. Assaud, C. Kryschi, B. Capon, C. Detavernier, L. Santinacci and J. Bachmann, Antimony sulfide as a light absorber in highly ordered, coaxial nanocylindrical arrays: preparation and integration into a photovoltaic device, *J. Mater. Chem. A*, 2015, **3**, 5971–5981.
25 Y. Itzhaik, O. Niitsoo, M. Page and G. Hodes, Sb_2S_3-sensitized nanoporous TiO_2 solar cells, *J. Phys. Chem. C*, 2009, **113**, 4254–4256.
26 J. Zhang, Z. Liu and Z. Liu, Novel WO_3/Sb_2S_3 heterojunction photocatalyst based on WO_3 of different morphologies for enhanced efficiency in photoelectrochemical water splitting, *ACS Appl. Mater. Interfaces*, 2016, **8**, 9684–9691.
27 Y. T. Song, L. Y. Lin, Y. S. Chen, H. Q. Chen, Z. D. Ni, C. C. Tu and S. S. Yang, Novel TiO_2/Sb_2S_3 heterojunction with whole visible-light response for photoelectrochemical water splitting reactions, *RSC Adv.*, 2016, **6**, 49130–49137.
28 Y. C. Pu, G. Wang, K. D. Chang, Y. Ling, Y. K. Lin, B. C. Fitzmorris, C. M. Liu, X. Lu, Y. Tong, J. Z. Zhang and Y. J. Hsu, Au nanostructure-decorated TiO_2 nanowires exhibiting photoactivity across entire UV-visible region for photoelectrochemical water splitting, *Nano Lett.*, 2013, **13**, 3817–3823.
29 H. J. Kim, S. H. Lee, A. A. Upadhye, I. Ro, M. I. Tejedor-Tejedor, M. A. Anderson, W. B. Kim and G. W. Huber, Plasmon-enhanced photoelectrochemical water splitting with size-controllable gold nanodot arrays, *ACS Nano*, 2014, **8**, 10756–10765.
30 X. Shi, K. Ueno, T. Oshikiri, Q. Sun, K. Sasaki and H. Misawa, Enhanced water splitting under modal strong coupling conditions, *Nat. Nanotechnol.*, 2018, **13**, 953–958.
31 H. Li, Z. Li, Y. Yu, Y. Ma, W. Yang, F. Wang, X. Yin and X. Wang, Surface-plasmon-resonance-enhanced photoelectrochemical water splitting from Au-nanoparticle-decorated 3D TiO_2 nanorod architectures, *J. Phys. Chem. C*, 2017, **121**, 12071–12079.
32 K. Qian, B. C. Sweeny, A. C. Johnston-Peck, W. Niu, J. O. Graham, J. S. DuChene, J. Qiu, Y. C. Wang, M. H. Engelhard, D. Su and E. A. Stach, Surface plasmon-driven water reduction: gold nanoparticle size matters, *J. Am. Chem. Soc.*, 2014, **136**, 9842–9845.
33 C. Peng, W. Wang, W. Zhang, Y. Liang and L. Zhuo, Surface plasmon-driven photoelectrochemical water splitting of TiO_2 nanowires decorated with Ag nanoparticles under visible light illumination, *Appl. Surf. Sci.*, 2017, **420**, 286–295.

34 Q. Wang, J. Qiao, X. Xu and S. Gao, Controlled synthesis of Cu nanoparticles on TiO_2 nanotube array photoelectrodes and their photoelectrochemical properties, *Mater. Lett.*, 2014, **131**, 135–137.

35 S. Linic, P. Christopher and D. B. Ingram, Plasmonic-metal nanostructures for efficient conversion of solar to chemical energy, *Nat. Mater.*, 2011, **10**, 911.

36 J. Li, S. K. Cushing, F. Meng, T. R. Senty, A. D. Bristow and N. Wu, Plasmon-induced resonance energy transfer for solar energy conversion, *Nat. Photonics*, 2015, **9**, 601.

37 P. V. Kamat and G. V. Hartland, Plasmons for Energy Conversion, *ACS Energy Lett.*, 2018, **3**, 1467–1469.

38 S. C. Warren and E. Thimsen, Plasmonic solar water splitting, *Energy Environ. Sci.*, 2012, **5**, 5133–5146.

39 X. Yang, H. Li, W. Zhang, M. Sun, L. Li, N. Xu, J. Wu and J. Sun, High visible photoelectrochemical activity of Ag nanoparticle-sandwiched CdS/Ag/ZnO nanorods, *ACS Appl. Mater. Interfaces*, 2017, **9**, 658–667.

40 J. Li, S. K. Cushing, P. Zheng, T. Senty, F. Meng, A. D. Bristow, A. Manivannan and N. Wu, Solar hydrogen generation by a CdS–Au–TiO_2 sandwich nanorod array enhanced with Au nanoparticle as electron relay and plasmonic photosensitizer, *J. Am. Chem. Soc.*, 2014, **136**, 8438–8449.

41 J. Toudert, R. Serna and M. Jimenez de Castro, Exploring the optical potential of nano-bismuth: tunable surface plasmon resonances in the near ultraviolet-to-near infrared range, *J. Phys. Chem. C*, 2012, **116**, 20530–20539.

42 F. Dong, T. Xiong, Y. Sun, Z. Zhao, Y. Zhou, X. Feng and Z. Wu, A semimetal bismuth element as a direct plasmonic photocatalyst, *Chem. Commun.*, 2014, **50**, 10386–10389.

43 W. Fan, C. Li, H. Bai, Y. Zhao, B. Luo, Y. Li, Y. Ge, W. Shi and H. Li, An in situ photoelectroreduction approach to fabricate Bi/BiOCl heterostructure photocathodes: understanding the role of Bi metal for solar water splitting, *J. Mater. Chem. A*, 2017, **5**, 4894–4903.

44 J. Wang, L. Tang, G. Zeng, Y. Liu, Y. Zhou, Y. Deng, J. Wang and B. Peng, Plasmonic Bi metal deposition and g-C_3N_4 coating on Bi_2WO_6 microspheres for efficient visible-light photocatalysis, *ACS Sustainable Chem. Eng.*, 2016, **5**, 1062–1072.

45 Z. Zhao, W. Zhang, Y. Sun, J. Yu, Y. Zhang, H. Wang, F. Dong and Z. Wu, Bi cocatalyst/Bi_2MoO_6 microspheres nanohybrid with SPR-promoted visible-light photocatalysis, *J. Phys. Chem. C*, 2016, **120**, 11889–11898.

46 B. R. Wulan, S. S. Yi, S. J. Li, Y. X. Duan, J. M. Yan, X. B. Zhang and Q. Jiang, Non-noble-metal bismuth nanoparticle-decorated bismuth vanadate nanoarray photoanode for efficient water splitting, *Mater. Chem. Front.*, 2018, **2**, 1799–1804.

47 Y. Li, L. Wei, R. Zhang, Y. Chen, L. Mei and J. Jiao, Annealing effect on Sb_2S_3–TiO_2 nanostructures for solar cell applications, *Nanoscale Res. Lett.*, 2013, **8**, 89.

48 D. U. Lee, S. Woo Pak, S. Gook Cho, E. Kyu Kim and S. Il Seok, Defect states in hybrid solar cells consisting of Sb_2S_3 quantum dots and TiO_2 nanoparticles, *Appl. Phys. Lett.*, 2013, **103**, 023901.

49 Z. Zhao, W. Zhang, X. Lv, Y. Sun, F. Dong and Y. Zhang, Noble metal-free Bi nanoparticles supported on TiO_2 with plasmon-enhanced visible light photocatalytic air purification, *Environ. Sci.: Nano*, 2016, **3**, 1306–1317.

50 Y. Chen, D. Chen, J. Chen, Q. Lu, M. Zhang, B. Liu, Q. Wang and Z. Wang, Facile synthesis of Bi nanoparticle modified TiO_2 with enhanced visible light photocatalytic activity, *J. Alloys Compd.*, 2015, **651**, 114–120.